

1 Studies of uniformity of 50 μm low-gain avalanche detectors
2 at the Fermilab test beam.

3 A. Apresyan^{*,a}, S. Xie^b, C. Pena^b, R. Arcidiacono^{e,g}, N. Cartiglia^e, M. Carulla^h,
4 G. Derylo^a, M. Ferrero^e, D. Flores^h, P. Freeman^d, Z. Galloway^d, A. Ghassemiⁱ, H. Al
5 Ghoul^c, L. Gray^a, S. Hidalgo^h, S. Kamadaⁱ, S. Los^a, M. Mandurrino^e, A. Merlos^h,
6 N. Minafra^c, A. Ronzhin^a, G. Pellegrini^h, D. Quirion^h, C. Royon^c, H. Sadrozinski^d,
7 A. Seiden^d, V. Sola^e, M. Spiropulu^b, A. Staiano^e, L. Uplegger^a, K. Yamamotoⁱ,
8 K. Yamamuraⁱ

9 ^a*Fermi National Accelerator Laboratory, Batavia, IL, USA*

10 ^b*California Institute of Technology, Pasadena, CA, USA*

11 ^c*University of Kansas, KS, USA*

12 ^d*SCIPP, University of California Santa Cruz, CA, USA*

13 ^e*INFN, Torino, Italy*

14 ^f*Università di Torino, Torino, Italy*

15 ^g*Università del Piemonte Orientale, Italy*

16 ^h*Centro Nacional de Microelectrónica (IMB-CNM-CSIC), Barcelona, Spain*

17 ⁱ*Hamamatsu Photonics (HPK), Hamamatsu, Japan*

18 **Abstract**

In this paper we report measurements of the uniformity of time resolution, signal amplitude, and charged particle detection efficiency across the sensor surface of low-gain avalanche detectors (LGAD). Comparisons of the performance of sensors with different doping concentrations and different active thicknesses are presented, as well as their temperature dependance and radiation tolerance up to $6 \times 10^{14} \text{ n/cm}^2$. Results were obtained at the Fermilab test beam facility using 120 GeV proton beams, and a high precision pixel tracking detector. LGAD sensors manufactured by the Centro Nacional de Microelectrónica (CNM) and Hamamatsu Photonics (HPK) were studied. The uniformity of the sensor response in pulse height before irradiation was found to have a 2% spread. The signal detection efficiency and timing resolution in the sensitive areas before irradiation were found to be 100% and 30-40 ps, respectively. A “no-response” area between pads was measured to be about 70 μm for CNM and 110 μm for HPK sensors. After a neutron fluence of $6 \times 10^{14} \text{ n/cm}^2$ the CNM sensor exhibits a large gain variation of up to a factor of 2.5 when comparing metallized and non-metallized sensor areas. An irradiated CNM sensor achieved a time resolution of 30 ps for the metallized area and 40 ps for the non-metallized area, while a HPK sensor irradiated to the same fluence achieved a 30 ps time resolution.

19 **Key words:**

20 Silicon, Timing, LGAD, Test Beam

21	Contents		
22	1	Introduction	2
23	2	Experimental Setup	3
24	3	LGAD Sensor Properties	5
25	4	Readout Electronics	7
26	5	Timestamp Reconstruction	7
27	6	Sensor Studies and Analysis	8
28	6.1	Study of the uniformity of the LGAD sensors	9
29	6.2	Measurement of the “no-response” area between two neighboring pixels . .	11
30	6.3	Comparison of HPK doping profiles	12
31	6.4	Comparison of uniformity of HPK 50 μm with 80 μm	15
32	6.5	Temperature dependence of the LGAD sensors	17
33	6.6	Radiation tolerance of the LGADs	20
34	7	Conclusion	22

35 1. Introduction

36 Future colliders, including the high luminosity upgrade of the Large Hadron Collider
37 (HL-LHC) at CERN, will operate with an order of magnitude higher instantaneous lu-
38 minosity compared to what has been achieved at the large hadron collider (LHC) so
39 far. With the increased instantaneous luminosity, the rate of simultaneous interactions
40 per bunch crossing (pileup) is projected to reach an average of 140 to 200. The large
41 amount of pileup increases the difficulties in separating particles from the hard scatter-
42 ing interaction with those produced in different pileup interactions. In particular, the
43 ability to discriminate between jets produced in the events of interests, especially those
44 associated with vector boson fusion processes, and jets produced by pileup interactions
45 will be degraded. Additionally, the efficiency to identify high p_{T} isolated electrons and
46 muons will be severely reduced due to the high density of pileup particles in their vicinity.
47 The missing transverse energy resolution will also deteriorate, and several other physics
48 objects performance metrics will also suffer the detrimental effects of pileup.

49 One way to mitigate the pileup effects mentioned above, complementary to precision
50 tracking methods, is to perform a time of arrival measurement associated with each par-
51 ticle. Such a measurement with a precision of about 30-40 ps, will reduce the effective
52 amount of pileup by a factor of 10, given that the spread in collision time of the pileup
53 interactions at HL-LHC is foreseen to be approximately 200 ps. It has been previously
54 shown that a precision of better than 20 ps can be achieved for electromagnetic showers

*Corresponding author
Email address: apresyan@fnal.gov (A. Apresyan)

measured with silicon sampling calorimeters [1–3] using traditional planar silicon detectors. In this paper, we report results of particle beam measurements with thin low-gain avalanche detectors (LGAD) that have been shown to achieve time resolutions around 30 ps [4?]. LGAD are envisioned to be used in the CMS and ATLAS experiment upgrades for HL-LHC in order to overcome the event reconstruction challenges posed by the high rate of concurrent collisions per beam crossing. The implemented regions of pseudorapidity (η) are: $|\eta| > 1.5$, and $2.4 < |\eta| < 4.2$ for CMS and ATLAS, respectively. In order to achieve the desired timing precision across a large area of the detectors, the sensors will need to provide high uniformity of signal response and timing resolution. In this paper, we perform detailed measurements of the performance of LGAD sensors produced by Centro Nacional de Microelectrónica (CNM) and Hamamatsu Photonics (HPK) exposed to the 120 GeV proton beam at Fermilab. Utilizing high-precision tracking detectors we extract position dependence of the charged-particle detection efficiency, signal pulse height, signal timestamp, and time resolution of 50 μm LGAD sensors. We also compare the uniformity of 50 and 80 μm LGAD sensors. Uniformity and time resolution of the HPK and CNM sensors irradiated to an equivalent neutron fluence of $6 \times 10^{14} \text{ n/cm}^2$ are also presented. Detailed measurements of irradiated HPK sensors were presented in Ref. [?].

The paper is organized as follows: the experimental setup is described in Sec. 2; the tested LGAD sensors and their operating conditions are listed in Sec. 3; readout electronics used in the measurements are described in Sec. 4; algorithms used in the event reconstruction are described in Sec. 5; beam test results are presented in Sec. 6, followed by the conclusion in Sec. 7.

2. Experimental Setup

Test-beam measurements were performed at the Fermilab Test-beam Facility (FTBF) which provided a 120 GeV proton beam from the Fermilab Main Injector accelerator. The Devices Under Test (DUTs) were mounted on a remotely operated motorized stage, placed inside the pixel telescope detector [5]. The latter provides better than 10 μm position resolution for charged particles impinging on the DUT. Additionally, a Photek 240 micro-channel plate (MCP-PMT) detector [6–9] was placed furthest downstream, and provided a very precise reference timestamp. Its precision has been previously measured to be less than 7 ps [8]. A schematic diagram and photograph of the experimental area are shown in Fig. 1 and Fig. 2, respectively.

The DAQ system for the DUTs and the Photek MCP-PMT is based on a CAEN V1742 digitizer board [10], which provides digitized waveforms sampled at 5 GS/s, and with one ADC count corresponding to 0.25 mV. The CAEN digitizer was voltage- and time-calibrated using the procedure described in Ref. [11]. One of the main parameters of DAQ system for precise time measurements is the “electronic time resolution”, defined as the measured time jitter between two signals that are split from the same source. These two signals are used as “start” and “stop” signals to electronic system measuring the time interval between them. The electronic time resolution of the CAEN V1742 digitizer was measured to be less than 4 ps, and thus, its impact on the timing measurements presented in these studies can be neglected. The DAQ for the pixel telescope is based on the CAPTAN system developed at Fermilab [5]. The track-reconstruction is performed using the Monicelli software package developed specifically for the test-beam application.

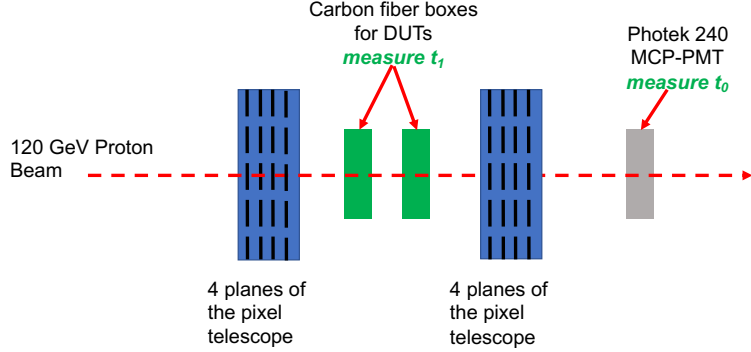


Figure 1: A schematic diagram of the test-beam setup is shown. The t_0 and t_1 are defined in Section 4.

100 The DUTs were placed inside the telescope box described in Ref.[5], and mounted on
 101 an aluminum mechanical support structure. The telescope box can be moved remotely
 102 in both the horizontal and vertical directions in order to align the DUTs with the beam.
 103 The aluminum support structure for the DUTs provide both mechanical stability and
 104 are equipped with Peltier cooling elements that were used in this study to operate the
 105 DUTs at -10° and -20° C.

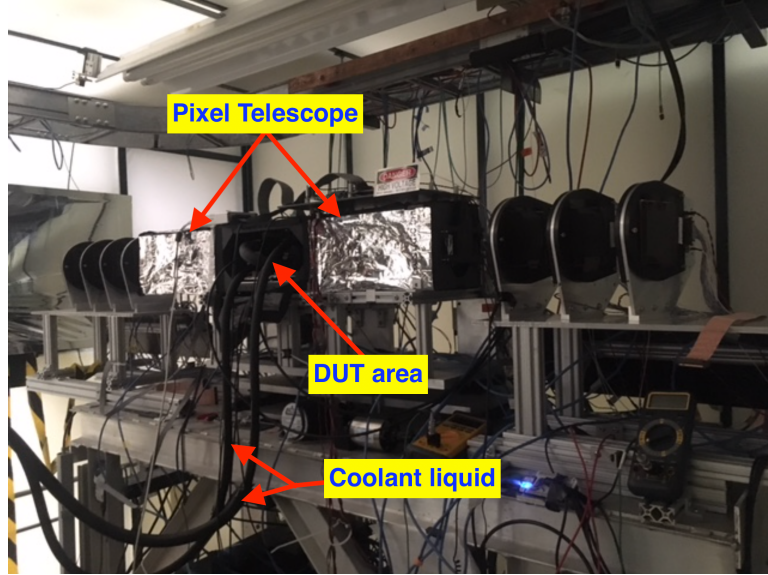


Figure 2: A picture of the experimental area. The pixel telescope detectors are placed inside the electrostatic-discharge shielded boxes on the two sides of the DUT area. Cooling liquid for the Peltier elements inside the DUT area is provided by the two tubes shown in the picture.

106 The beam is resonantly extracted in a slow spill for each Main Injector cycle delivering
 107 a single 4.2 sec long spill per minute. The primary beam (bunched at 53 MHz) consists

108 of 120 GeV protons. All measurements presented in this paper were taken with the
 109 primary beam particles. The trigger to both the CAEN V1742 and to the pixel telescope
 110 was provided by a scintillator mounted on a photomultiplier tube, placed upstream of
 111 the DUTs in the beam-line. Due to the limited buffer depth of the CAEN V1742 board,
 112 special care had to be taken in the design of the DAQ system to ensure that both the DUT
 113 and telescope DAQs collect exactly the same amount of triggers. This was achieved by
 114 limiting the trigger rate by introducing an adjustable dead-time using a custom-designed
 115 trigger board. This trigger board is the combination of a custom FPGA board (the
 116 CAPTAN+x, equipped with multiple FPGA Mezzanine Card connectors and gigabit
 117 ethernet connectivity) mated to a front end board (the NIM+, with multiple inputs and
 118 outputs, each supporting a variety of interface levels such as NIM, LVDS, and TTL).
 119 The combined board is shown in Fig. 3 and was used to interface to photomultiplier
 120 signals through on-board programmable discriminators, and to form trigger signals with
 121 software configurable time-based veto and pre-scaler event filtering. We found that at a
 122 rate of about 1,500 triggers per spill the CAEN V1742 and pixel telescope maintained
 123 full synchronization. Processed data from the pixel telescope and the DUTs were merged
 124 offline by matching the trigger counters recorded by the two systems.



Figure 3: The custom-made trigger board composed of NIM+ and CAPTAN+x boards.

125 3. LGAD Sensor Properties

126 Sensors manufactured by HPK and CNM were measured in the test beam experiment.
 127 Both single- and four-channel configurations of the sensor were used in the measurements.
 128 The sensors studied have active thicknesses of about 50 μm and 80 μm .

129 CNM sensors have an active thickness of about 45 μm and were produced on 4-inch
 130 Silicon-on-Insulator wafers with a 45 μm thick high resistivity float zone (FZ) active layer
 131 on top of a 1 μm buried oxide and a 300 μm support wafer. The back-side contact is

132 achieved through wet-etched deep access holes through the insulator. Details on CNM
133 sensors can be found in Ref. [4, 12].

134 The HPK sensors were manufactured on 6-inch silicon wafers of $150\ \mu\text{m}$ total thickness
135 with a $50\ \mu\text{m}$ or $80\ \mu\text{m}$ thick high resistivity float zone (FZ) active layer. Four gain splits,
136 identified with the letters A (lowest gain) to D (highest gain), were produced identical
137 in the mask design but with a different p^+ dose of the gain layer to study the optimal
138 parameters for fast timing detectors. The pads were produced in three versions: two with
139 guard ring (GR and GBGR) and one without guard ring. Four-channel sensors in a 2×2
140 array were produced with all 4 gain-splits, and are identified with the PIX identifier. For
141 example, the 2×2 array of the $50\ \mu\text{m}$ sensor split D is labelled as 50D-PIX. The sensor
142 corresponding to each of the four channels in the array is also referred to as a pixel in
143 this paper. Each pixel in the 2×2 HPK array has dimensions of $3 \times 3\ \text{mm}^2$. The CNM
144 single-channel sensors are square pads with an active area of $1.7\ \text{mm}^2$ while the HPK
145 single-channel sensors are circular pads with an active area of $0.8\ \text{mm}^2$.

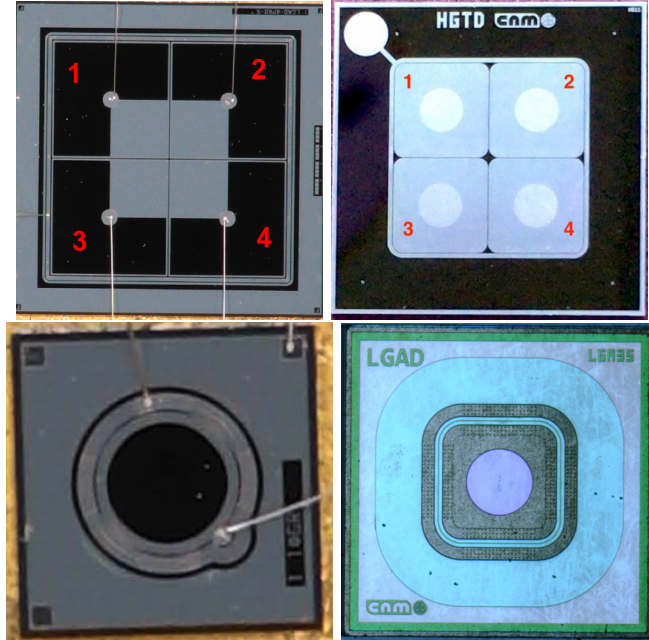


Figure 4: Photographs of the HPK 50D-PIX 2×2 array sensor (top left), the CNM W9HG11 2×2 array sensor (top right), the HPK 50D-GR single sensor (bottom left), and the CNM W11LGA35 single sensor (bottom right) are shown. Numerical labels overlaid on top of the images of the array sensors are used in the text when referring to individual pixels.

146 **4. Readout Electronics**

147 Three readout electronics boards were used in various measurements presented in this
148 paper. They were independently developed at Fermi National Accelerator Laboratory
149 (FNAL), at the University of Kansas (KU), and at the University of California Santa
150 Cruz (UCSC).

Sensor	Number of channels	Single channel dimensions	Single channel capacitance
HPK 50A-PIX	4	$3 \times 3 \text{ mm}^2$	20 pF
HPK 50B-PIX	4	$3 \times 3 \text{ mm}^2$	20 pF
HPK 50C-PIX	4	$3 \times 3 \text{ mm}^2$	20 pF
HPK 50D-PIX	4	$3 \times 3 \text{ mm}^2$	20 pF
HPK 80C-PIX	4	$3 \times 3 \text{ mm}^2$	12 pF
HPK 50D	1	$\varnothing = 1.0 \text{ mm}$	2.9 pF
CNM-W9HG11	4	$3 \times 3 \text{ mm}^2$	22 pF
CNM-W11LGA35	1	$1.3 \times 1.3 \text{ mm}^2$	3.9 pF

Table 1: Linear dimensions and capacitances of the sensors used in these studies.

151 The 4-channel Fermilab LGAD test board is designed to test sensors up to 8.5 mm
 152 by 8.5 mm at voltages up to 1 kV. Four wire-bonding pads allow for signal readout
 153 via amplifiers based on Mini-Circuits GALI-66+. The amplifiers feature transformers
 154 with 1:2 input impedance matching, two stages of amplification and a 500 MHz low-
 155 pass filter. In this full configuration, the amplifiers feature 12.5Ω input impedance, $5 \text{ k}\Omega$
 156 transimpedance, 500 MHz bandwidth and 1 mV rms output noise. If needed it is possible
 157 to jump the input transformer and/or the low-pass filter, which would result in an input
 158 impedance of 50Ω , transimpedance of $10 \text{ k}\Omega$, and bandwidth of 2 GHz.

159 The 2-channel KU board, designed and produced by the University of Kansas, can
 160 accommodate many types of sensors including diamond, silicon, LGAD or avalanche
 161 photodiodes (APD). The sensor is hosted on the board itself and the electronics was
 162 optimized for precise timing measurements. In particular, the amplifier, made with
 163 discrete components, has an input impedance of 700Ω , an output noise of 4 mV and a
 164 gain in transresistance of about $50 \text{ mV}/\mu\text{A}$ with a 3 dB bandwidth of 100 MHz. Those
 165 values were simulated for an input capacitance of 20 pF, which corresponds roughly to
 166 an LGAD of 9 mm^2 . The power consumption of the board is about 130 mW per channel.

167 The UCSC 1-channel board is described in detail in Ref. [4]. This board uses discrete
 168 components and contains several features which allow for maintaining a wide bandwidth
 169 ($\sim 2 \text{ GHz}$) and a low noise even in noisy environments. The inverting amplifier uses a
 170 high-speed SiGe transistor which has a transimpedance of about 470Ω . A commercial
 171 inverting amplifier with gain 10x is used to boost the signal. The 4-channel UCSC board
 172 has two stages: the first one is identical to the UCSC single channel board, and is followed
 173 by an inverting stage. The total transimpedance is $10.7 \text{ k}\Omega$.

174 5. Timestamp Reconstruction

175 As discussed in Section 2, the reference time is measured using the Photek MCP-
 176 PMT detector. The timestamp for this reference detector is obtained by fitting the peak
 177 region of the pulse to a Gaussian function and the mean parameter of the Gaussian is
 178 assigned as the timestamp t_0 . A more detailed description can be found in Ref [6].

179 The timestamp for signals from the LGAD sensors is obtained in two different ways
 180 depending on which read-out board was used. For the KU board, which has a slower
 181 decay time, the timestamp is obtained by performing a linear fit to the rising edge of
 182 the pulse, between 15% and 70% of the maximum amplitude, and the time at which
 183 the pulse reaches 45% of the maximum amplitude is assigned as its timestamp t_1 . We
 184 refer to this algorithm as the constant fraction discriminator (CFD) method. For the

185 FNAL and UCSC boards, which have fast decay times, the timestamp is obtained via
 186 a fit to a Gaussian function analogous to what is done for the reference detector. This
 187 procedure is slightly different compared to previous studies of LGAD sensors, where the
 188 CFD method was used uniformly.

189 The choices of the timestamp reconstruction algorithms listed above were motivated
 190 by the result of a dedicated study of various algorithms for each of the three readout
 191 boards. The study is performed using signals from the HPK 50D sensor. Constant
 192 fraction discriminant (CFD) and constant threshold discriminant (CTD) algorithms are
 193 used and the time resolution performance is studied as a function of the threshold used. In
 194 Tables 2 and 3, we show the time resolution obtained for different thresholds for the CFD
 195 and CTD algorithms respectively, for the KU readout board. For the CFD algorithm, we
 196 observed no significant dependence of the timestamp on the pulse height of the signal.
 197 However, for the CTD algorithm, the timestamp does depend on the pulse height and
 198 requires a correction referred to as a time-walk correction. For most situations, the time-
 199 walk correction can be accurately described by a linear dependence of timestamp on
 200 pulse height, however we do observe that as the CTD threshold increases, the time-walk
 201 correction becomes more quadratic. In Table 3, the time resolution is reported for both
 202 linear and quadratic time-walk corrections. We observe that the best results are obtained
 203 for a CFD threshold at 45%. However the CTD algorithm at a moderate threshold does
 204 yield comparable time resolutions.

CFD Threshold	Time Resolution
15%	45 ps
30%	40 ps
45%	38 ps
60%	39 ps

Table 2: Time resolution measured for the HPK 50D-PIX sensor on the KU readout board using the constant fraction discriminant algorithm.

CTD Threshold	Time Resolution (Linear Time-walk Correction)	Time Resolution (Quadratic Time-walk Correction)
12 mV	52 ps	51 ps
18 mV	46 ps	45 ps
24 mV	43 ps	42 ps
37 mV	41 ps	40 ps
49 mV	43 ps	39 ps
61 mV	43 ps	39 ps
73 mV	45 ps	40 ps

Table 3: Time resolution measured for the HPK 50D-PIX sensor on the KU readout board using the constant threshold discriminant algorithm.

205 In Table 4, we show the analogous study performed for the FNAL and UCSC readout
 206 boards. As signals on these readout boards have fast decay times, the Gaussian fit yields
 207 the best performance. As for the KU readout board, the CFD and CTD algorithms again
 208 give similar performance for the FNAL and UCSC readout boards.

Timestamp Algorithm Type	Time Resolution (FNAL Board with (HPK 50D-PIX Sensor)	Time Resolution (UCSC Board with irradiated HPK 50D Sensor)
Gaussian Fit	42 ps	35 ps
CFD at 15% Threshold	71 ps	47 ps
CFD at 30% Threshold	60 ps	42 ps
CFD at 45% Threshold	53 ps	39 ps
CFD at 60% Threshold	56 ps	44 ps
CTD at 18 mV Threshold (Linear Time-walk Correction)	55 ps	43 ps
CTD at 18 mV Threshold (Quadratic Timewalk Correction)	52 ps	37 ps

Table 4: Time resolution measured for the HPK 50D-PIX sensor on the FNAL readout board and the irradiated HPK 50D sensor on the UCSC board for a variety of timestamp reconstruction algorithms.

209 6. Sensor Studies and Analysis

210 We present a number of different studies performed on the LGAD sensors described
 211 in Section 3. They include signal response uniformity, gap distance between adjacent
 212 pixels, doping profile and sensor thickness characterization, temperature and irradiation
 213 dependence, and time resolution. A brief overview of the analysis methods is given below,
 214 followed by subsections describing the details and results of each study.

215 Events are required to have a signal in the Photek MCP-PMT consistent with a
 216 minimum ionizing particle (MIP), and a signal above the noise in LGAD sensors. The
 217 signal selection in the Photek MCP-PMT is the same for all runs and requires that the
 218 signal is consistent with a MIP corresponding to amplitude values in the range between
 219 160 mV and 320 mV. Signal events in LGAD sensors are selected such that they are
 220 above the noise levels listed for each board in Sec. 4. All measurements other than those
 221 described in Sec. 6.5 and 6.6 were performed at room temperature.

222 Here, and in the remainder of this article, whenever a scan of a certain characteristic
 223 quantity – e.g. time resolution – of the sensor is presented, we show the X-axis scan for
 224 pixels 1 and 2, and the Y-axis scan for pixels 1 and 3, as defined on the left picture in
 225 Fig. 4. The X-axis scan across pixels 3 and 4, and Y-axis scan across pixels 2 and 4 show
 226 qualitatively the same features, and are not presented here. Measurements presented
 227 for various sensors were obtained from different datasets and therefore the statistical
 228 precision is not always the same. The reason that in some measurements the error bars
 229 are not the same across either X- or Y-coordinate is due to the fact that the beam does
 230 not uniformly illuminate the whole sensor area, and hence the number of events is not
 231 the same across sensor surface.

232 6.1. Study of the uniformity of the LGAD sensors

233 We present in detail uniformity studies – including signal detection efficiency, most
 234 probable value, time difference, and time resolution – across the sensitive area of the
 235 LGAD. The sensors under study were produced by HPK and CNM. The largest dataset
 236 was collected for the HPK 50D-PIX and the CNM W9HG11 sensors. The HPK 50D-PIX
 237 sensor was mounted on the 4-channel FNAL board and biased to -300 V, while the CNM
 238 W9HG11 sensor was mounted on the 4-channel UCSC board and biased to -180 V. Both
 239 sensors were operated at room temperature for these studies.

240 The measurements of the particle detection efficiency are shown in Fig. 5. Efficiency
 241 is defined as the ratio of events that register a signal above the noise level to those that
 242 contain a track identified by the pixel telescope pointing at the LGAD sensor. Error bars
 243 in all efficiency measurements are evaluated as Clopper-Pearson intervals for calculating
 244 binomial confidence intervals. Noise values for different boards used in the experiments
 245 are listed in Sec. 4, and were measured using dedicated runs with no particles, and
 246 data collected using random triggers. Signals used in the efficiency measurements were
 247 required to have amplitude above 20 mV plots, well above the noise level.

248 We observe a flat 100% efficiency across the whole sensor area. The left edge in the
 249 X-axis scan of pixel 1 on HPK 50D-PIX sensor in Fig. 5 is outside the acceptance of the
 250 pixel telescope, hence the efficiency curve does not fully cover its surface. A clear drop
 251 in efficiency is observed in the transition (“no-response”) region between the two pixels.
 252 A more detailed study of the “no-response” region is given in Sec. 6.2.

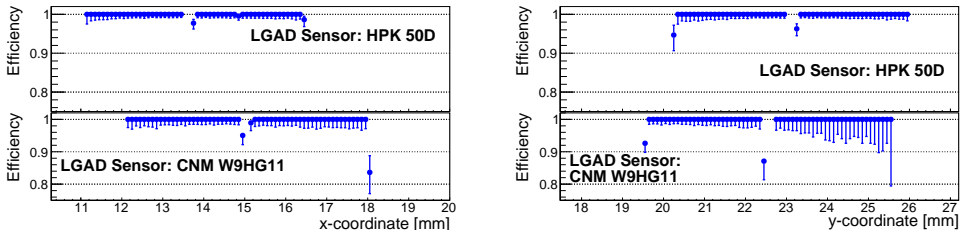


Figure 5: Efficiency measurement across the X-axis (left) and Y-axes (right) of the HPK 50D-PIX sensor mounted on the FNAL board, and the CNM W9HG11 sensor mounted on the UCSC board. The scans of pixels 1 and 2 along the X-axis, and pixels 1 and 3 along the Y-axis are shown. The pixel numbering scheme is defined in Fig. 4.

253 An important characteristic is the uniformity of the signal size across the surface of the
 254 sensor, which directly impacts on its timing performance. We use the signal amplitude
 255 as the metric to characterize the signal size uniformity. The distribution of the LGAD
 256 signal amplitudes is fitted to a Landau distribution. The most probable value (MPV)
 257 parameter of the fitted Landau distribution is plotted in Fig. 6. A flat response with a
 258 uniform signal size is observed over the whole sensor area.

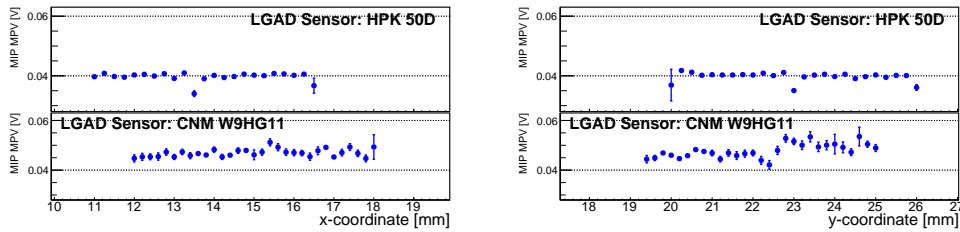


Figure 6: Signal amplitude MPV measurement across the X-axis (left) and Y-axes (right) of the HPK 50D-PIX sensor mounted on the FNAL board, and the CNM W9HG11 sensor mounted on the UCSC board. The scans of pixels 1 and 2 along the X-axis and pixels 1 and 3 along the Y-axis are shown. The pixel numbering scheme is defined in Fig. 4.

259 The measurements of the time difference $\Delta t = t_1 - t_0$ between the reference timestamp
 10

(t_0) and the timestamp of the LGAD sensors (t_1) are shown in Fig. 7. The micro-bonding scheme of the HPK and CNM 2×2 sensor arrays is shown in Fig. 4. For the HPK sensor, the Δt dependence on the hit position indicates a shift of about 20–30 ps between the metallized area near the center of the array (gray region of the top-left image in Fig. 4) and the non-metallized area. A possible explanation for this effect is a small difference in the rise time of the pulses that originate from the passage of particles in the metallized and non-metallized areas. This effect cannot be attributed to the algorithm used to time-stamp the events, since the same behavior is observed with the CFD and CDT algorithms. Furthermore, the same behavior is observed on all HPK sensor varieties mounted on KU board, as presented in Sec. 6.3. The CNM W9HG11 sensor does not contain metallized areas on its surface and we do not observe the same effect.

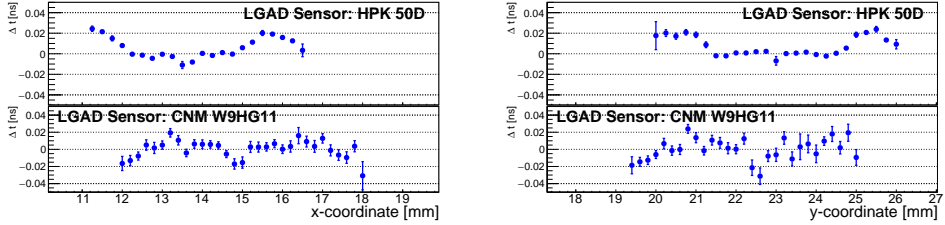


Figure 7: Δt measurement across the X- and Y-axes of the HPK 50D-PIX sensor mounted on the FNAL board, and the CNM W9HG11 sensor mounted on the UCSC board. The scans of pixels 1 and 2 along the X-axis, and pixels 1 and 3 along the Y-axis are shown. The pixel numbering scheme is defined in Fig. 4.

The measurement of the time resolution across the sensor surface is shown in Fig. 8. The distribution of Δt between the timestamp of the LGAD signal and the reference signal is fitted with a Gaussian function, and the spread σ of the fitted function is defined as the time resolution. We observe a uniform time resolution around 40 ps across the whole surface area for HPK, and around 55 ps for CNM sensors.

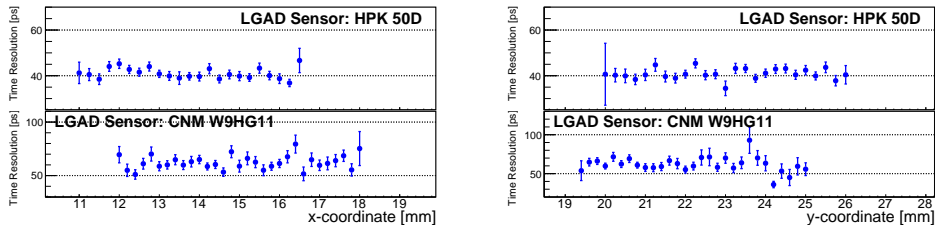


Figure 8: Time resolution measurement across the X-axis (left) and Y-axes (right) of the HPK 50D-PIX sensor mounted on the FNAL board, and the CNM W9HG11 sensor mounted on the UCSC board. The scans of pixels 1 and 2 along the X-axis, and pixels 1 and 3 along the Y-axis are shown. The pixel numbering scheme is defined in Fig. 4.

6.2. Measurement of the “no-response” area between two neighboring pixels

In order to precisely measure the width of the no-response area between two neighboring pixels, a large statistics sample of about 350,000 events was collected with the

279 HPK 50D-PIX sensor mounted on a 2-channel KU board. The sensor was biased to
 280 -300 V. The large dataset allowed us to perform a detailed scan in the area between
 281 the two pixels as shown in Fig. 9. In order to estimate the width of the no-response
 282 between the pixels, the efficiency curves of the two neighboring pixels are fitted with an
 283 S-curve function of the form $y = p_1 \times \text{Erf}\{\pm(p_2 - x)/p_3\} + p_4$, where $\text{Erf}\{x\}$ is the error
 284 function defined as:

$$\text{Erf}(x) = \frac{2}{\sqrt{\pi}} \times \int_0^x e^{-t^2} dt \quad (1)$$

285 , and p_i were free parameters of the fit. We define the width of the “no-response” area as
 286 the distance between the half-maxima of the two fitted S-curves, as shown in Fig. 9. We
 287 measure the width of the no-response area on the HPK 50D-PIX sensor to be $110 \mu\text{m}$,
 288 with an uncertainty of $10 \mu\text{m}$. Data points outside the sensor area in Figs. 9, 10 actually
 289 had hit the sensor active area, but the coordinate of the track is incorrectly assigned,
 290 due to a small probability ($< 1\%$) to misreconstruct the position of the track.

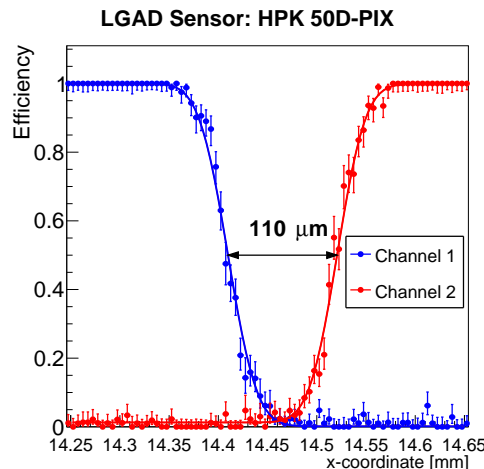


Figure 9: A zoom-in version of the efficiency measurement as a function of the X position of the beam particle. The HPK 50D-PIX sensor was operated at -300 V bias voltage. The pixel numbering scheme is defined in Fig. 4.

291 A further measurement was made on the 4-channel UCSC board for the HPK 50C-
 292 PIX sensor and the CNM W9HG11 sensor. We compare the width of the gap region of
 293 the HPK and CNM sensors in Fig. 10. Both sensors in this comparison were tested in
 294 the beam simultaneously. The HPK 50C-PIX sensor was operated at -450 V, and CNM
 295 W9HG11 sensor was operated at -180 V. We measure the size of the “no-response”
 296 region to be around $110 \mu\text{m}$ on the HPK 50C-PIX – compatible with the HPK 50D-PIX
 297 sensor – and around $70 \mu\text{m}$ for the CNM sensor. Both measurements have an uncertainty
 298 of $10 \mu\text{m}$.

299 6.3. Comparison of HPK doping profiles

300 Studies of the dependence of the sensors’ characteristics on the doping concentrations
 301 were performed by comparing the $50 \mu\text{m}$ HPK PIX sensors of different gain splits.

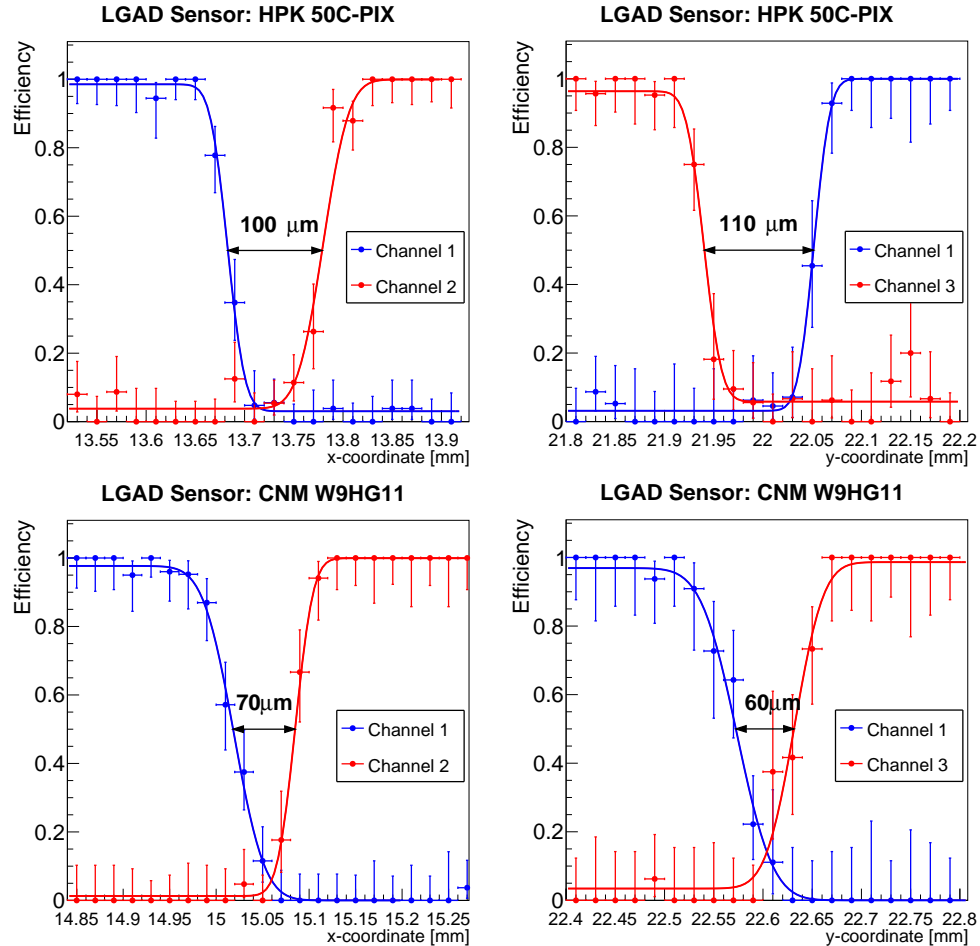


Figure 10: A zoom-in version of the efficiency measurement across the X- and Y-axes of the HPK 50C-PIX (top) and CNM W9HG11 (bottom) sensors. HPK sensor is operated at -450 V, and CNM sensor is operated at -180 V. Data points in blue are those from one pixel, and data points in red are from the neighboring pixel. The blue and red curves are fitted to the data points as described in the text. Arrows indicate the distance between the half-maximum points of the fitted curves.

302 In order to reduce the impact of the variations between different readout boards, all
303 measurements presented in this section were performed using only 2-channel KU readout
304 boards. Four readout boards were prepared, each with an HPK sensor mounted on it, and
305 tested in the beam. Data taken with the HPK 50D-PIX is the same as that presented
306 in Fig. 9, which is the largest data sample collected during this test beam campaign.
307 Therefore, the statistical uncertainties in the measurements of the HPK 50A-, B-, and
308 C-PIX sensors are larger than those of 50D-PIX. For this study, the sensors were oper-
309 ated at room temperature, and their bias voltages were set to -630 V, -550 V, -400 V,
310 and -300 V for the HPK 50A-PIX, HPK 50B-PIX, HPK 50C-PIX, and HPK 50D-PIX
311 sensors, respectively.

312 The distribution of the MPV of signal amplitudes across the sensor area is shown
313 in Fig. 11, where the MPV is extracted as described in Sec. 6.1. Comparing the signal
314 amplitudes between the two pixels we observe that the average amplitude varies between
315 the two channels. However, in Fig. 6 we observed that the amplitudes in the two pixels
316 of the same HPK 50D-PIX sensor on the FNAL readout board do not show the same
317 variations. We conclude that the observed difference in amplitude is due to imperfec-
318 tions in the manufacturing process of the custom-designed pre-amplifiers used in the KU
319 readout board and not due to sensor properties. Nevertheless, the signal MPV within a
320 single pixel is highly uniform for all tested samples.

321 The measurements of the time difference between the reference timestamp and the
322 timestamps of the HPK sensors are shown in Fig. 12. As was shown in Fig. 7, the Δt
323 exhibits an offset of about 20 ps between the metallized area and the non-metallized area
324 of the sensor. The feature is present in all 4 types of the HPK PIX sensors, does not
325 depend on the readout board or timestamp reconstruction algorithm used, and appears
326 to be statistically consistent in shape and magnitude.

327 The measurements of the time resolution across the sensors are shown in Fig. 13. We
328 observe a uniform time resolution around 40 ps across the entire sensor area.

329 6.4. Comparison of uniformity of HPK 50 μm with 80 μm

330 The thickness of the active area of the sensor is an important design parameter when
331 optimizing for time resolution. A detailed study of time resolution of HPK sensors of 80
332 and 50 μm is presented in [?]. Here we compare the uniformity of the time resolution
333 across the sensors of these two thicknesses. This study is performed using the HPK
334 C-PIX sensors with the same dopant concentration. The 80 μm sensor HPK 80C-PIX
335 is biased at -610 V, while the 50 μm sensor HPK 50C-PIX is biased at -400 V. The
336 sensors's gains at these bias voltages are: about 11 for the 80 μm sensor, and about 14
337 for the 50 μm sensor. The time resolution for the two sensors are shown in Fig. 14 as
338 a function of position, and exhibit fairly uniform behavior. Measurements of the HPK
339 50C-PIX sensor were performed on the KU 2-channel board, and those for HPK 80C-PIX
340 used the FNAL 4-channel board.

341 6.5. Temperature dependence of the LGAD sensors

342 In order to maintain their optimal performance at the highest fluences envisioned at
343 the HL-LHC, the LGAD sensors will be cooled to temperatures below -20°C degrees.
344 Operation at such low temperatures will allow to significantly reduce the leakage current,
345 and additionally improve the timing characteristics of the sensors. In this section we de-
346 scribe the measurements of the LGAD sensors performed at -10 and -20°C degrees, and

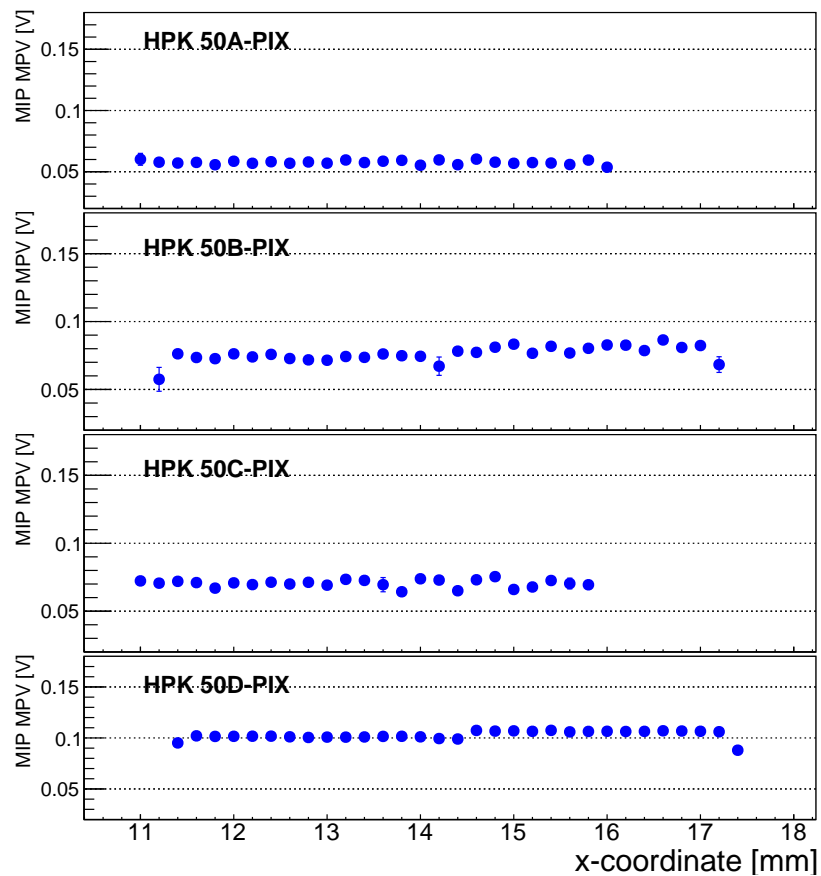


Figure 11: Signal amplitude MPV measurement across the X-axis of the HPK 50A-, 50B-, 50C-, and 50D-PIX sensors mounted on the KU board. The scan of pixels 1 and 2 along the X-axis, and pixel numbering scheme is defined in Fig. 4.

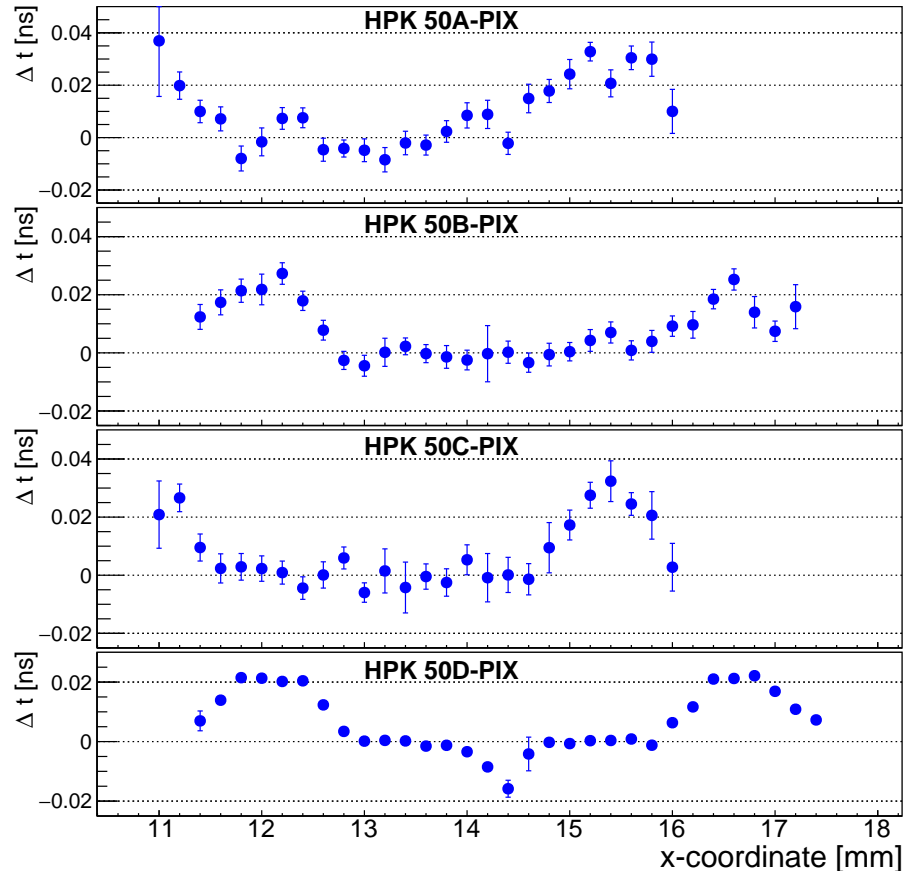


Figure 12: Δt measurements as a function of the X position of the beam particle for the HPK 50A-, 50B-, 50C-, and 50D-PIX sensors mounted on the KU board. The scan of pixels 1 and 2 along the X-axis is shown. The pixel numbering scheme is defined in Fig. 4.

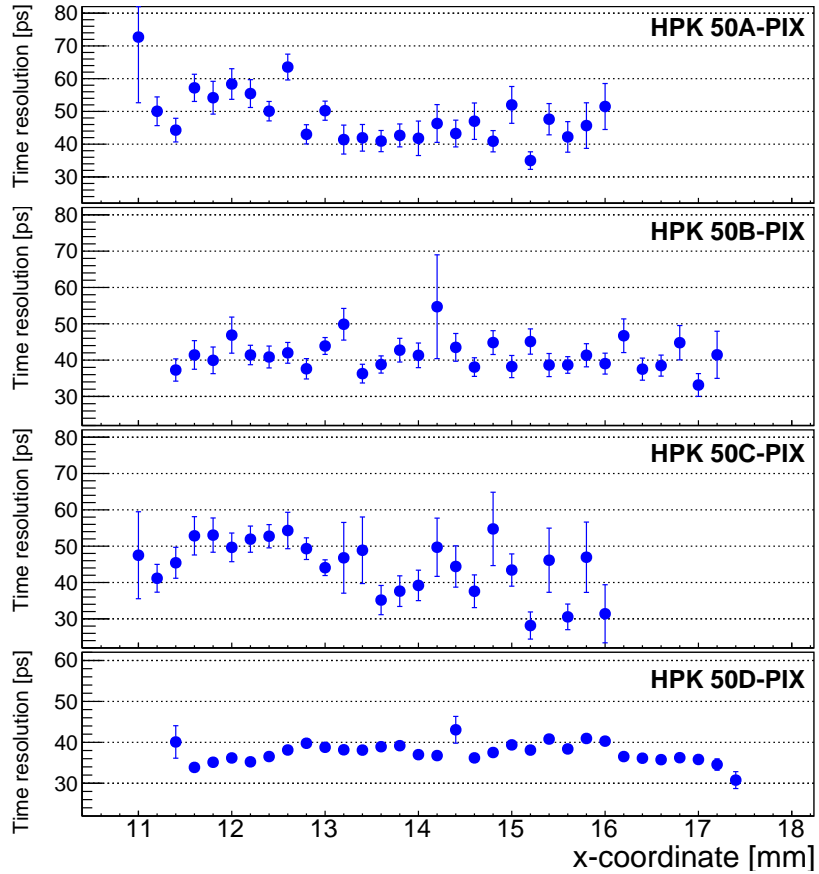


Figure 13: Time resolution measurements as a function of the X position of the beam particle for the HPK 50A-, 50B-, 50C-, and 50D-PIX sensors mounted on the KU board. The scan of pixels 1 and 2 along the X-axis is shown. The pixel numbering scheme is defined in Fig. 4.

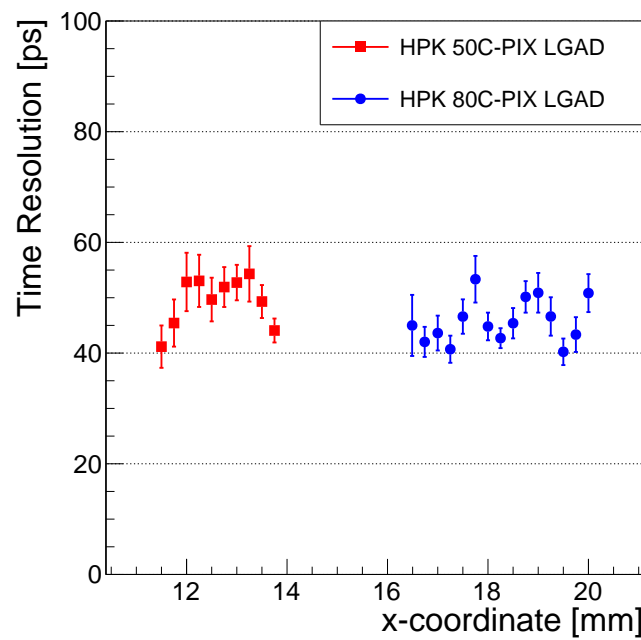


Figure 14: Comparison of the uniformity of the measured time resolution of the HPK 80C-PIX versus 50C-PIX sensors. The 80 μm sensor is mounted on the FNAL board, and is biased at -610 V, and the 50 μm sensor is mounted on the KU board and is biased at -400 V.

347 compare the results to those at room temperature. These measurements were performed
 348 with the HPK 50D-PIX sensors mounted on the FNAL 4-channel board. The sensor was
 349 biased at the same voltage of -250 V for all temperature scenarios. The HPK 50D gain
 350 at this bias voltage and at $+20^{\circ}\text{C}$ was measured to be 15, while at -20°C and the same
 351 bias voltage it was measured to be 25.

352 The distribution of the signal MPV across the sensor surface is shown in Fig. 15. We
 353 observe that the signal MPV increases by more than a factor of two when the temperature
 354 is reduced from $+20^{\circ}\text{C}$ to -20°C . While the MPV uniformity across the two channels
 355 are within 2% of each other at room temperature, at lower temperatures one of the pixels
 356 shows a difference of about 5% with respect to its neighboring pixel. A more detailed
 357 study is needed to understand whether this difference is due to non-uniform temperature
 358 distribution across the sensor array or due to differences in the signal response between
 359 different pixel sensors at colder temperatures.

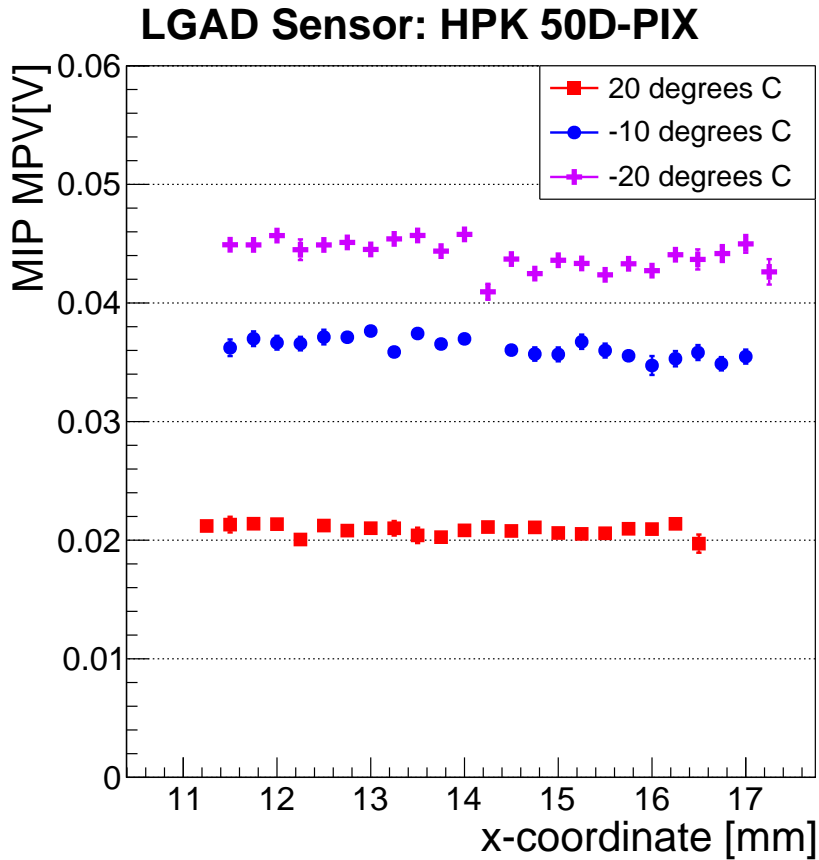


Figure 15: Temperature dependance of the signal amplitude MPV uniformity across the X-axis of the HPK 50D-PIX sensors mounted on the FNAL board. The scan of pixels 1 and 2 along the X-axis is shown, and pixel numberng scheme is defined in Fig. 4. The HPK sensor is biased at -250 V.

360 The distribution of the Δt between the reference timestamp and the timestamp from
 19

³⁶¹ the HPK 50D-PIX sensor is shown in Fig. 16. We observe no significant changes in the
³⁶² behavior of the Δt as the temperature varies.

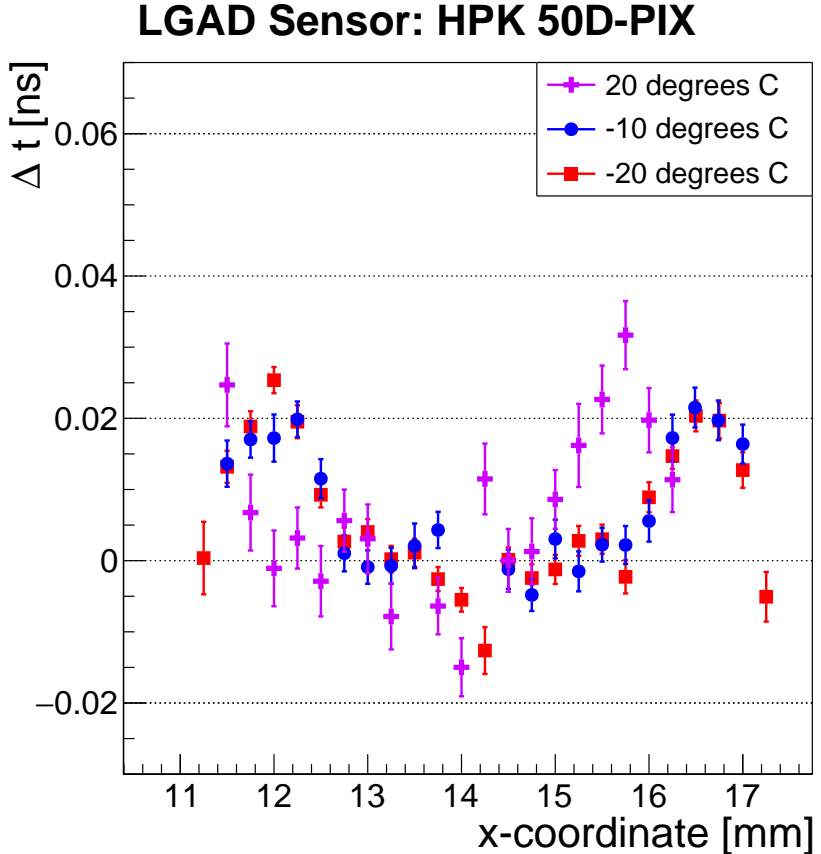


Figure 16: Temperature dependance of the Δt uniformity across the X-axis of the HPK 50D-PIX sensors mounted on the FNAL board. The scan of pixels 1 and 2 along the X-axis is shown, and pixel numbering scheme is defined in Fig. 4. The HPK sensor is biased at -250 V.

³⁶³ The time resolution measured for the HPK 50D-PIX sensor is shown in Fig. 17. We
³⁶⁴ observe a significant improvement in the time resolution as the temperature is lowered
³⁶⁵ from $+20^{\circ}\text{C}$ to -20°C degrees. As the temperature is lowered, the signal-to-noise ratio
³⁶⁶ improves as the gain of the LGAD sensor increases. Generally, the electronic noise may
³⁶⁷ also decrease as the temperature is lowered, but in our case it was observed to remain
³⁶⁸ relatively constant at 1.2 mV for both $+20$ and -20°C . Therefore the improvement comes
³⁶⁹ mainly from the increase in the signal gain. The time resolution was measured to improve
³⁷⁰ from around $55\text{-}60$ ps at the room temperature, down to $35\text{-}40$ ps at -20°C . It is worth
³⁷¹ noting that time resolution around 35 ps with pixels of area 9 mm^2 is a promising result
³⁷² for cost-effective implementation in LHC experiments.

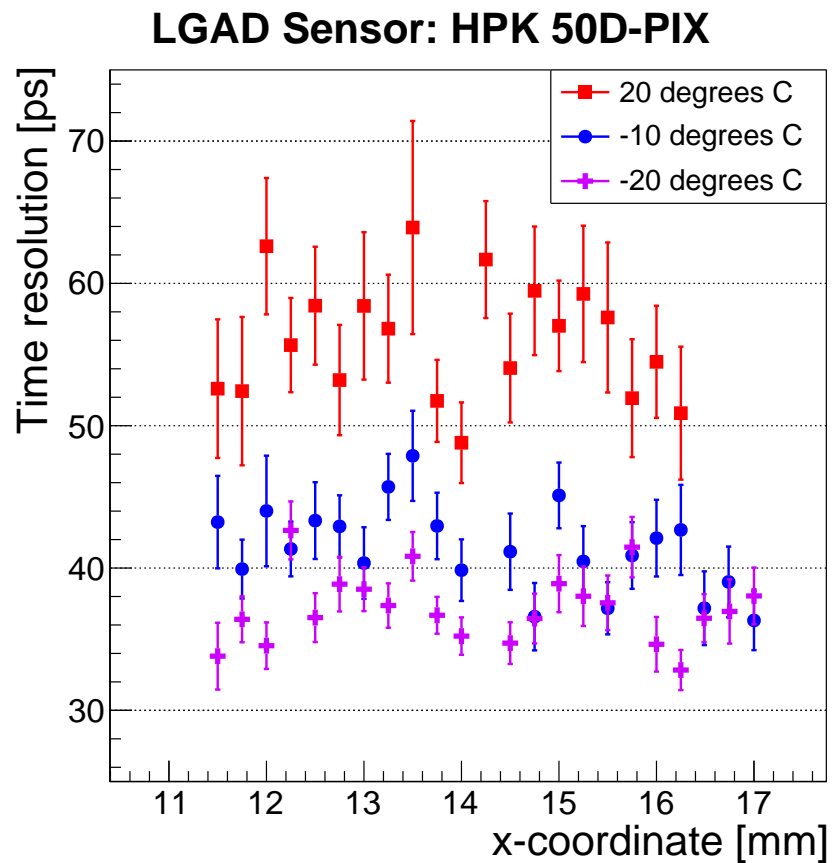


Figure 17: Temperature dependance of the time resolution uniformity across the X-axis of the HPK 50D-PIX sensors mounted on the FNAL board. The scan of pixels 1 and 2 along the X-axis is shown. The pixel numberng scheme is defined in Fig. 4. The HPK sensor is biased at -250 V.

373 **6.6. Radiation tolerance of the LGADs**

374 In this section we present the studies of the irradiated HPK and CNM sensors, which
 375 were exposed to neutron irradiation at the Ljubljana TRIGA reactor. The neutron
 376 spectrum and flux are well known and the fluence is quoted in 1 MeV equivalent neutrons
 377 per cm² ($n_{eq.}/cm^2$ or n/cm² for short). After 6×10^{14} n/cm² irradiation, the devices
 378 were annealed for 80 min at 60°C. Afterward the devices were kept at -20°C degree
 379 during storage, transportation, and test beam experiments.

380 The two-dimensional distribution of the signal amplitudes on the surface of the ir-
 381 radiated sensors are shown in Figs. 18 and 19. From the comparison with the image
 382 of the CNM sensor shown in Fig. 4 and the distribution in Fig. 18, it is clear that two
 383 distinct regions can be identified on the sensor based on the signal amplitude: the region
 384 under the aluminum metallization on the periphery of the sensor, and the region without
 385 aluminum metallization in the center. The distribution on the right of Fig. 18 shows
 386 that the amplitude under the aluminum (periphery) is about 2.5 times larger than that
 387 without aluminum (center). The amplitude scan of the irradiated HPK 50D sensor is
 388 shown on the left panel of Fig. 19, and a uniform amplitude across the sensor surface
 389 is observed, which can also be seen on the right panel of Fig. 19. In contrast to the
 390 CNM sensor, the whole surface of the active area of the HPK 50D sensor is covered with
 391 aluminum metallization.

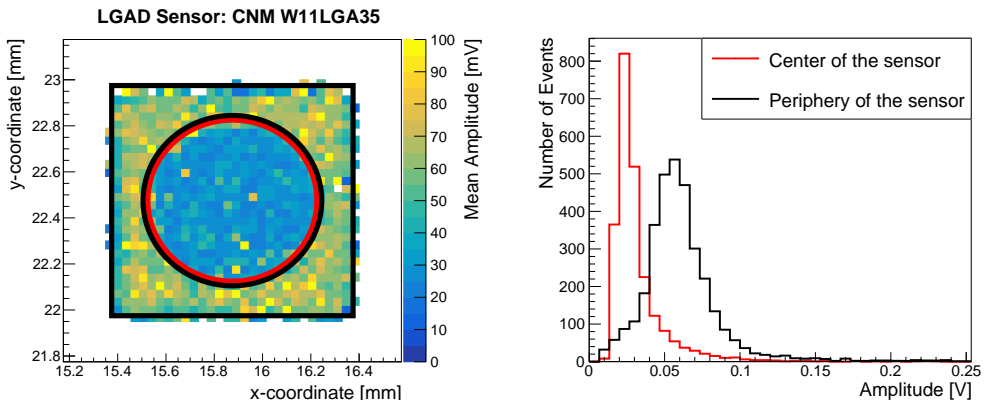


Figure 18: (Left) The map of the amplitude distribution on the irradiated CNM W11LGA35 sensor across X and Y coordinates. Two distinct regions on the sensor surface can be identified according to the amplitude distribution: the center of the sensor (area within the red circle), and the periphery of the sensor (area between the black circle and black square). (Right) Amplitude distribution in the two areas of the irradiated CNM W11LGA35 sensor. The sensor was irradiated to 6×10^{14} n/cm². Measurements were performed at -20°C.

392 Measurements of the particle detection efficiency are shown in Fig. 20. These mea-
 393 surements were performed with the HPK sensor biased at -600 V, and the CNM sensor
 394 biased at -400 V. We observe a flat 100% efficiency across the whole HPK sensor area,
 395 and the efficiency of the CNM sensor is also very close to 100%. As with the pixelated
 396 array sensors, a clear drop in efficiency is observed near the edges of the active area.

397 The distribution of MPV of signal amplitudes across the sensor area is shown in
 398 Fig. 21, where the MPV is extracted as described in Sec. 6.1. Measurements were per-

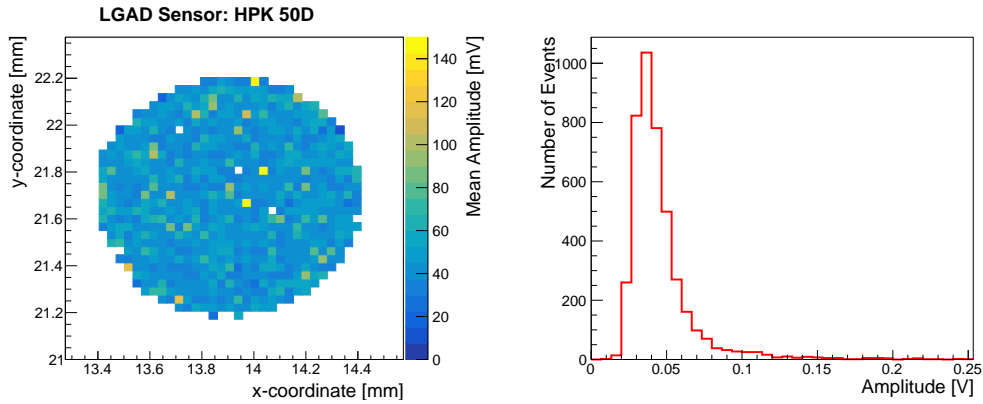


Figure 19: (Left) The map of the amplitude distribution on the irradiated HPK 50D sensor across X and Y coordinates. (Right) Signal amplitude distribution for the irradiated HPK 50D sensor. The sensor was irradiated to 6×10^{14} n/cm². Measurements were performed at -20°C .

399 formed at two bias voltage values for both sensors: -600 and -635 V for HPK (gain
400 equal to 19 and 29, respectively), and -400 and -420 V for CNM sensors (gain equal to
401 14 and 15, respectively). A uniform signal amplitude is observed across the HPK sensor,
402 while for the CNM sensor the amplitude varies across the sensor surface, as observed also
403 in Fig. 18.

404 The distribution of the Δt between the reference timestamp and the timestamps of the
405 signals from the irradiated HPK and CNM sensors are shown in Fig. 22. Measurements
406 at both bias voltage values are presented. We measured a uniform distribution of the
407 Δt values across the HPK sensor. The CNM sensor exhibits a non-uniformity across the
408 sensor surface, where the signals from the central, non-metallized area arrive about 10 ps
409 earlier than those from the peripheral, metallized area.

410 Distributions of the time resolution across the surface of the irradiated sensors are
411 shown in Fig. 23. The time resolution measured with the HPK sensor improves slightly
412 with the increase of the bias voltage, and shows a uniform distribution across the sensor
413 surface. In contrast, the CNM sensor shows a non-uniform distribution of time resolution,
414 which is a consequence of the variations of the signal amplitude across the sensor. We
415 do not observe an improvement in the time resolution measured with the CNM sensor
416 with the increase in the bias voltage.

417 7. Conclusion

418 In a beam test at FNAL with tracking information, we compared the performance
419 of LGAD produced by CNM Barcelona and HPK Hamamatsu. Single pads of diameter
420 1 mm and 2×2 arrays of square pixels of 3 mm were used. Sensors with thicknesses of
421 about 50 and 80 μm were studied. The uniformity of the sensor response in pulse height,
422 efficiency, and timing resolution were studied. Four different readout boards were used
423 in these studies. The uniformity of the sensor response in pulse height before irradiation
424 was found to have a 2% spread. The efficiency and timing resolution before irradiation
425 were found to be 100% and 30-40 ps, respectively. The “non-response” region between

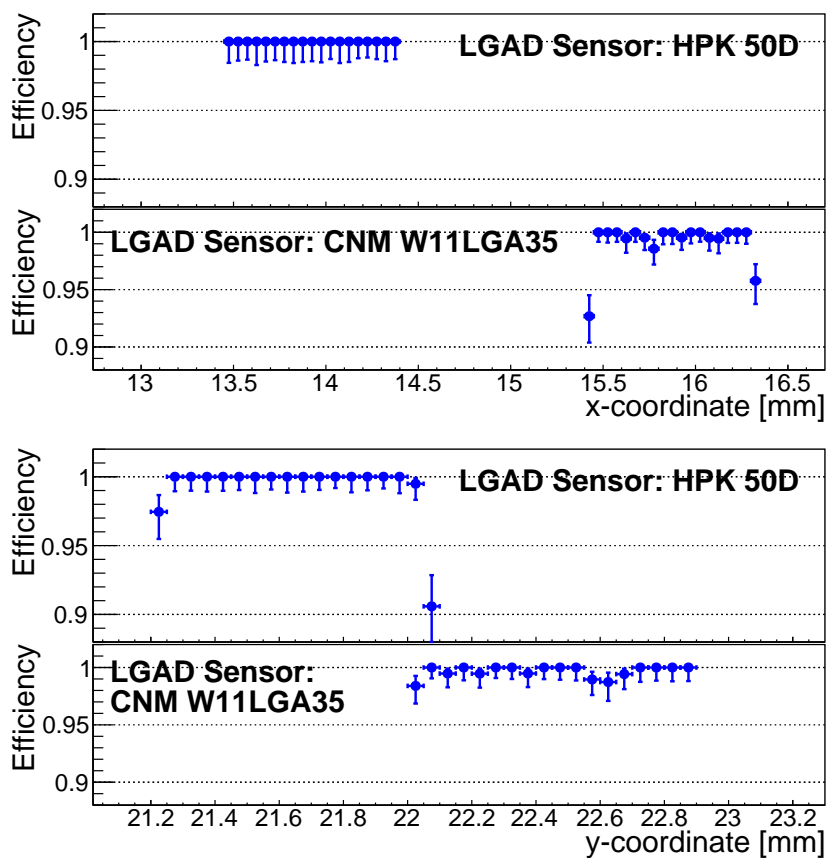


Figure 20: Efficiency measurements across the X-axis (top) and Y-axes (bottom) of the HPK 50D and CNM W11LGA35 irradiated sensors. Both sensors were irradiated to $6 \times 10^{14} \text{ n/cm}^2$. Measurements were performed at -20°C .

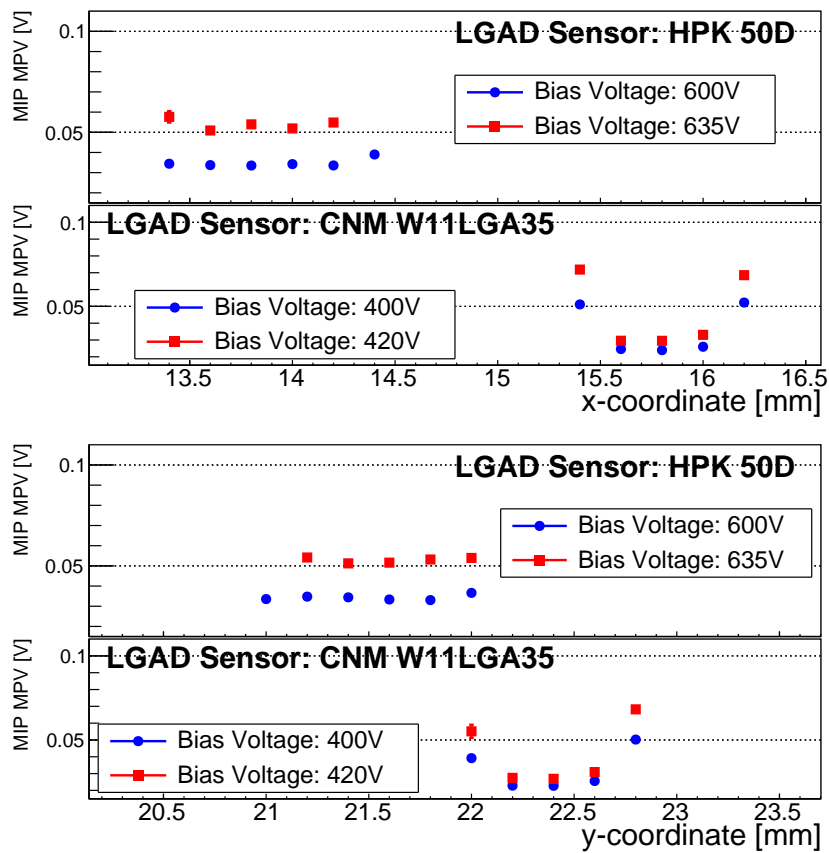


Figure 21: Signal amplitude MPV measurement across the X-axis (top) and Y-axes (bottom) of the HPK 50D and CNM W11LGA35 irradiated sensors. Both sensors were irradiated to $6 \times 10^{14} \text{ n/cm}^2$. Measurements were performed at -20°C .

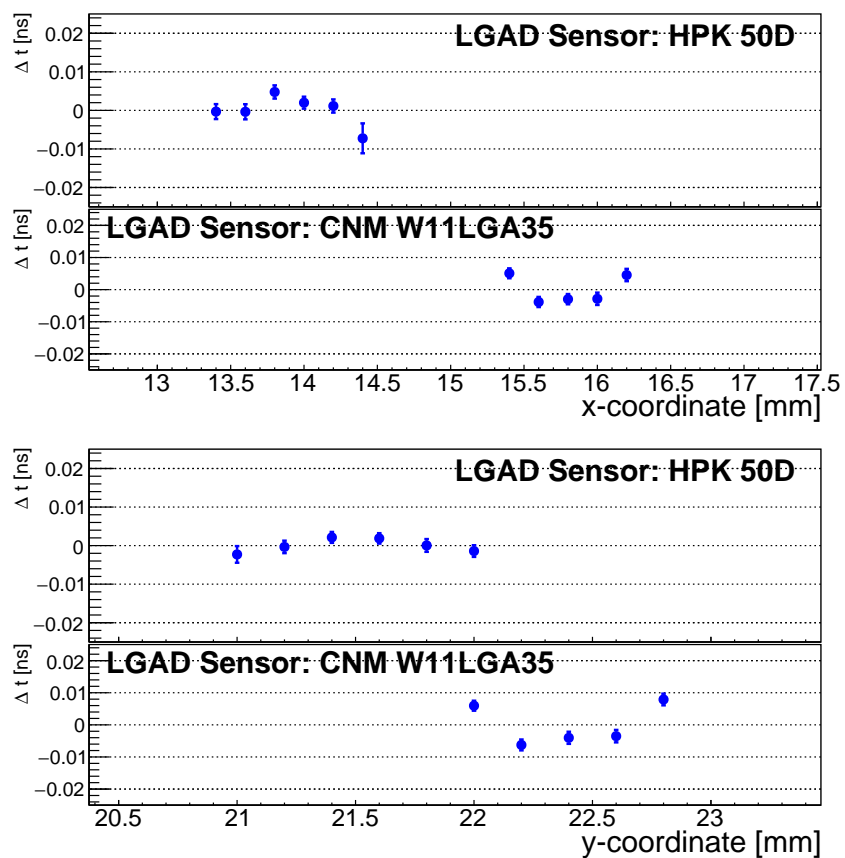


Figure 22: Δt measurements across the X-axis (top) and Y-axes (bottom) of the HPK 50D and CNM W11LGA35 irradiated sensors. Both sensors were irradiated to 6×10^{14} n/cm². Measurements were performed at -20°C .

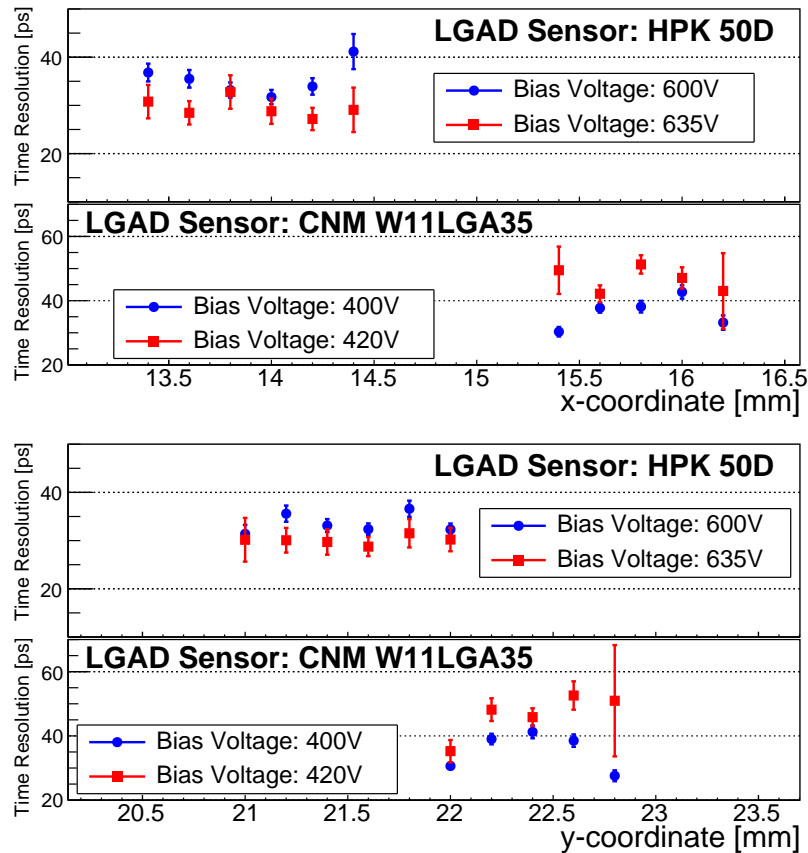


Figure 23: Time resolution measurements across the X-axis (top) and Y-axes (bottom) of the HPK 50D and CNM W11LGA35 irradiated sensors. Both sensors were irradiated to $6 \times 10^{14} \text{ n/cm}^2$. Measurements were performed at -20°C .

426 pixels was measured to be about $70\text{ }\mu\text{m}$ for CNM sensors and $110\text{ }\mu\text{m}$ for HPK sensors. A
427 small timing shift across the HPK sensor of the order $20\text{--}30\text{ ps'}$ can be explained by the
428 observed change in pulse shape when comparing metallized and non-metallized sensor
429 areas. Uniform signal detection efficiency of 100% is observed on all sensors, both before
430 and after irradiation.

431 For an un-irradiated $50\text{ }\mu\text{m}$ thick LGADs with 3 mm pads we find the following timing
432 results:

- 433 • at a temperature of $+20^\circ\text{C}$, the timing resolution ranges from 40 ps to 50 ps
434 depending on the readout board.
- 435 • cooling the LGAD, while keeping the bias voltage the same at -250 V , improves
436 the timing resolution from 55 ps at $+20^\circ\text{C}$ to 43 ps at -10°C to 36 ps at -20°C .

437 After a neutron fluence of $6 \times 10^{14}\text{ n/cm}^2$, the single pad CNM sensor exhibits a
438 large gain variation of a factor 2.5 when comparing metallized and non-metallized sensor
439 areas. For an $50\text{ }\mu\text{m}$ thick LGAD with 1 mm pads irradiated $6 \times 10^{14}\text{ n/cm}^2$ we find the
440 following timing results when operated at -20°C :

- 441 • for the HPK LGAD the highest bias voltage reached is -635 V and the correspond-
442 ing timing resolution is 30 ps;
- 443 • for the CNM LGAD the highest bias voltage reached is -420 V and the correspond-
444 ing timing resolution is 30 ps for the metallized area and 40 ps for the non-metallized
445 area.

446 Acknowledgement

447 We thank the FTBF personnel and Fermilab accelerator's team for very good beam
448 conditions during our test beam time. We also appreciate the technical support of the
449 Fermilab SiDet department for the rapid production of wire-bonded and packaged LGAD
450 assemblies. We would like to thank Alan Prosser and Ryan Rivera for their critical help
451 in setting up the DAQ and trigger chain. We thank Ned Spencer, Max Wilder, and Forest
452 McKinney-Martinez for their technical assistance, and the CNM and HPK manufacturing
453 team. We acknowledge the help of V. Cindro and I. Mandic with the neutron irradiations.

454 This document was prepared using the resources of the Fermi National Accelerator
455 Laboratory (Fermilab), a U.S. Department of Energy, Office of Science, HEP User Facility.
456 Fermilab is managed by Fermi Research Alliance, LLC (FRA), acting under Contract
457 No. DE-AC02-07CH11359. Part of this work was performed within the framework of
458 the CERN RD50 collaboration.

459 This work was supported by the Fermilab LDRD 2017.027; by the United States
460 Department of Energy grant DE-FG02-04ER41286; by the California Institute of Tech-
461 nology High Energy Physics under Contract DE-SC0011925; by the European Union's
462 Horizon 2020 Research and Innovation funding program, under Grant Agreement no.
463 654168 (AIDA-2020) and Grant Agreement no. 669529 (ERC UFSD669529); by the
464 Italian Ministero degli Affari Esteri and INFN Gruppo V; and by the Spanish Min-
465 istry of Economy, Industry and Competitiveness through the Particle Physics National
466 Program (ref. FPA2014-55295-C3-2-R and FPA2015-69260-C3-3-R) co-financed with
467 FEDER funds.

468 **References**

- 469 [1] A. Apresyan, G. Bolla, A. Bornheim, H. Kim, S. Los, C. Pena, E. Ramberg, A. Ronzhin, M. Spiropulu, and S. Xie, "Test beam studies of silicon timing for use in calorimetry," *Nuclear Instruments and Methods in Physics Research Section A: Accelerators, Spectrometers, Detectors and Associated Equipment*, vol. 825, pp. 62 – 68, 2016.
- 470 [2] A. Apresyan, "Investigation of Fast Timing Capabilities of Silicon Sensors for the CMS High Granularity Calorimeter at HL-LHC," in *Proceedings, 2016 IEEE Nuclear Science Symposium and Medical Imaging Conference (NSS/MIC 2016)*, Oct 2016. <http://2016.nss-mic.org/index.php>.
- 471 [3] N. Akchurin, V. Ciriolo, E. Currs, J. Damgov, M. Fernández, C. Gallrapp, L. Gray, A. Junkes, M. Mannelli, K. M. Kwok, P. Meridiani, M. Moll, S. Nourbakhsh, S. Pigazzini, C. Scharf, P. Silva, G. Steinbrueck, T. T. de Fatis, and I. Vila, "On the timing performance of thin planar silicon sensors," *Nuclear Instruments and Methods in Physics Research Section A: Accelerators, Spectrometers, Detectors and Associated Equipment*, vol. 859, pp. 31 – 36, 2017.
- 472 [4] N. Cartiglia *et al.*, "Beam test results of a 16 ps timing system based on ultra-fast silicon detectors," *Nucl. Instrum. Meth. A*, vol. 850, pp. 83 – 88, 2017.
- 473 [5] G. Pellegrini, P. Fernández-Martínez, M. Baselga, C. Fleta, D. Flores, V. Greco, S. Hidalgo, I. Mandić, G. Kramberger, D. Quirion, and M. Ullan, "Technology developments and first measurements of Low Gain Avalanche Detectors (LGAD) for high energy physics applications," *Nuclear Instruments and Methods in Physics Research Section A: Accelerators, Spectrometers, Detectors and Associated Equipment*, vol. 765, pp. 12 – 16, 2014. HSTD-9 2013 - Proceedings of the 9th International.
- 474 [6] Z. Galloway *et al.*, "Properties of HPK UFSD after neutron irradiation up to 6e15 n/cm²," 2017. arXiv/1707.04961 [physics.ins-det].
- 475 [7] S. Kwan, C. Lei, D. Menasce, L. Moroni, J. Ngadiuba, A. Prosser, R. Rivera, S. Terzo, M. Turqueti, L. Uplegger, L. Vigani, and M. E. Dinardo, "The pixel tracking telescope at the fermilab test beam facility," *Nuclear Instruments and Methods in Physics Research Section A: Accelerators, Spectrometers, Detectors and Associated Equipment*, vol. 811, pp. 162 – 169, 2016.
- 476 [8] D. Anderson, A. Apresyan, A. Bornheim, J. Duarte, C. Pena, A. Ronzhin, M. Spiropulu, J. Trevor, and S. Xie, "On Timing Properties of LYSO-Based Calorimeters," *Nucl. Instrum. Meth. A*, vol. 794, pp. 7–14, 2015.
- 477 [9] A. Ronzhin, S. Los, E. Ramberg, M. Spiropulu, A. Apresyan, S. Xie, H. Kim, and A. Zatserklyaniy, "Development of a new fast shower maximum detector based on microchannel plates photomultipliers (MCP-PMT) as an active element," *Nucl. Instrum. Meth. A*, vol. 759, pp. 65 – 73, 2014.
- 478 [10] A. Ronzhin, S. Los, E. Ramberg, A. Apresyan, S. Xie, M. Spiropulu, and H. Kim, "Study of the timing performance of micro-channel plate photomultiplier for use as an active layer in a shower maximum detector," *Nucl. Instrum. Meth. A*, vol. 795, pp. 288 – 292, 2015.
- 479 [11] A. Ronzhin, S. Los, E. Ramberg, A. Apresyan, S. Xie, M. Spiropulu, and H. Kim, "Direct tests of micro channel plates as the active element of a new shower maximum detector," *Nucl. Instrum. Meth. A*, vol. 795, pp. 52 – 57, 2015.
- 480 [12] <http://www.caen.it/csite/CaenProd.jsp?parent=11&idmod=661>.
- 481 [13] H. Kim, C.-T. Chen, N. Eclov, A. Ronzhin, P. Murat, E. Ramberg, S. Los, W. Moses, W.-S. Choong, and C.-M. Kao, "A new time calibration method for switched-capacitor-array-based waveform samplers," *Nucl. Instrum. Meth. A*, vol. 767, pp. 67 – 74, 2014.
- 482 [14] M. Carulli *et al.*, "First 50 m thick LGAD fabrication at CNM." <https://agenda.infn.it/getFile.py/access?contribId=20&sessionId=8&resId=0&materialId=slides&confId=11109>, 2016. 28th RD50 Workshop, Torino.
- 483
- 484
- 485
- 486
- 487
- 488
- 489
- 490
- 491
- 492
- 493
- 494
- 495
- 496
- 497
- 498
- 499
- 500
- 501
- 502
- 503
- 504
- 505
- 506
- 507
- 508
- 509
- 510
- 511
- 512
- 513